International Journal of Nanomedicine

Dovepress
Taylor & Francis Group

Open Access Full Text Article

ORIGINAL RESEARCH

A Hybrid Protein-Oxygen Nanomedicine Overcomes Osimertinib Resistance in NSCLC via HIF-1α/VEGF/EGFR Inhibition

Guanming Jiang[1,*], Xuyi Liu[2,3,*], Dou Zhang[2,3,*], Zhenying Diao[2,3], Xiaojun Yang[1], Qinquan Tan[1], Shiyuan Chen[1], Wan Zhang[1], Xiumao Yin[1], Ting Yin[2,3], Xiaozhen Wang[4], Jianping Zhou[5]

[1]Department of Oncology, Tenth Affiliated Hospital, Southern Medical University (Dongguan People's Hospital), Dongguan, Guangdong, 523059, People's Republic of China; [2]Research Center of Nano Technology and Application Engineering, The First Dongguan Affiliated Hospital, School of Pharmacy, Guangdong Medical University, Dongguan, Guangdong, 523808, People's Republic of China; [3]Dongguan Biomedical Nano Engineering Technology Research Center, Guangdong Medical University, Dongguan, Guangdong, 523808, People's Republic of China; [4]Respiratory department, Tsinghua University Yuquan Hospital, Beijing, 100040, People's Republic of China; [5]Department of Thoracic Surgery, Tenth Affiliated Hospital, Southern Medical University (Dongguan People's hospital), Dongguan, Guangdong, 523059, People's Republic of China

*These authors contributed equally to this work

Correspondence: Xiaozhen Wang, Respiratory Department, Tsinghua University Yuquan Hospital, Beijing, 100040, People's Republic of China, Email zhxiaowang@126.com; Jianping Zhou, Department of Thoracic Surgery, Tenth Affiliated Hospital, Southern Medical University (Dongguan People's Hospital), Dongguan, Guangdong, 523059, People's Republic of China, Email zhoujianping0165@smu.edu.cn

Purpose: Osimertinib, established as the frontline treatment for advanced non-small cell lung cancer (NSCLC), can effectively prolong progression-free survival. However, it faces the problem of reduced treatment persistence due to acquired drug resistance. Meanwhile, tumor hypoxia is also a key driver of drug resistance. This study proposes a hybrid protein oxygen nanocarrier combined with osimertinib and ginsenoside Rg3 to address the drug resistance issue of NSCLC through multiple mechanisms.

Methods: A hybrid protein-oxygen multifunctional nanoplatform (OG@HPO) was engineered by co-encapsulating OSI and GRg3 within oxygen-rich protein matrices. Initial confirmed the synthesis of OG@HPO and characterized its drug/oxygen release. Subsequent in vitro assays verified OG@HPO's tumoricidal activity and elucidated its mechanistic. Finally, in vivo evaluations validated the nanoplatform's tumor targeting and anticancer efficacy.

Results: Preliminary experiments confirmed successful OG@HPO preparation and validated its drug/oxygen release capacities. In vitro assays demonstrated the potent cytotoxic effects of OG@HPO against H1975 OR cells. In vivo biodistribution studies revealed excellent tumor-targeting of OG@HPO in H1975 OR xenograft mice. Subsequent 18 days therapeutic monitoring showed superior antitumor efficacy accompanied and favorable biosafety profile of OG@HPO. More importantly, in vitro and in vivo studies demonstrated that OG@HPO effectively oxygenate tumor microenvironment, thereby inhibiting hypoxia-driven HIF-1α expression and simultaneously inhibiting the vascular endothelial growth factor (VEGF)/EGFR pathway.

Conclusion: OG@HPO represents an innovative multifunctional nanoplatform integrating tumor-targeting, multi-drug delivery, and hypoxia modulation capabilities. By effectively alleviating tumor hypoxia, it achieves multiple inhibition of HIF-1α and EGFR/VEGF pathways. Ultimately, enhances NSCLC sensitivity to osimertinib, thereby reversing acquired resistance. Overall, OG@HPO is regarded as a promising strategy to overcome osimertinib resistance providing a clinically translatable solution.

Keywords: non–small cell lung cancer, osimertinib resistance, hypoxia-inducible factor, vascular endothelial growth factor, epidermal growth factor receptor

Introduction

Lung cancer remains the leading cause of cancer-related mortality globally, with non-small cell lung cancer (NSCLC) constituting approximately 85% of all diagnosed cases.[1,2] A critical molecular feature of NSCLC involves activating mutations within the epidermal growth factor receptor (EGFR) gene, most notably exon 19 deletions (19del) and exon 21

Received: 31 March 2025
Accepted: 15 August 2025
Published: 27 August 2025

L858R substitutions.[3–6] These genetic aberrations transduce signals that drive carcinogenesis through the tyrosine kinase structural domain. Consequently, EGFR-tyrosine kinase inhibitors (TKIs) have emerged as the first choice for NSCLC treatment.[7] Among these agents, osimertinib, the irreversible third-generation EGFR-TKI, has replaced earlier generations (such as erlotinib and afatinib) as the preferred treatment for EGFR-mutated patients. It is attributed to osimertinib has superior therapeutic prognosis and T790M mutation targeting.[8–11] However, 70–80% of patients inevitably develop acquired resistance within 24 months.[12,13] Therefore, overcoming the resistance of osimertinib remains a critical challenge that needs to be solved.

In order to overcome osimertinib resistance, multiple therapeutic paradigms have been investigated, including chemotherapy, immunotherapy and targeted therapies.[14–16] However, conventional chemotherapy often provides only transient disease control and is associated with substantial toxic burdens.[17,18] Immunotherapy can potentially produce durable efficacy in some patients, especially those with high PD-L1 expression, but tumors with EGFR mutations are less sensitive to immune checkpoint inhibitors.[19–21] Similarly, targeted therapies usually targets a specific target for treatment, whereas osimertinib resistance typically acquired by up-regulation or transformation of multiple alternative factors promoting value-added signalling pathways. This single-target therapy can limit the clinical benefit to the patient.[22–24] Emerging evidence implicates that tumor hypoxia may be an important driver in osimertinib resistance pathogenesis.[25] Activation of EGFR upregulates hypoxia-inducible factor-1α (HIF-1α), which transcriptionally regulates downstream targets, including promoting vascular endothelial growth factor (VEGF) expression, establishing a self-reinforcing cycle that drives tumor progression.[26,27] To address this multifactorial resistance, there is an urgent need to develop new drugs that improve the hypoxic state of the tumor microenvironment and disrupt hypoxic signaling. Meanwhile, they can synergistically target the resistance mechanisms to combat tumors. This integrated approach is expected to restore sensitivity to EGFR-targeted therapy and improve patient outcomes.

Here, an innovative nanotherapeutical strategy was developed that simultaneously disrupts the hypoxic tumor microenvironment and inhibits EGFR/VEGF pathways, ultimately overcoming NSCLC resistance to osimertinib for highly effective anti-tumor therapy (Scheme 1). Specifically, a hybrid protein oxygenate nanodrug (OG@HPO) was developed by co-coat osimertinib (OSI) and ginsenoside Rg3 (GRg3) with structural basis of human serum albumin (HSA) and hemoglobin (Hb). This nanosystem co-delivers OSI and GRg3 while achieving tumor-specific oxygen delivery through HSA-mediated targeting and intrinsic oxygen-carrying capacity of Hb.[28–30] When hypoxia in the tumor microenvironment is improved, HIF-1α expression is suppressed, and GRg3 down-regulates VEGF which ultimately blocking the HIF-1α/VEGF/EGFR pathway.[31,32] This dual-pronged approach not only enhances the antitumor efficacy of osimertinib in resistant NSCLC models but also delays the emergence of acquired resistance. Notably, the nanotherapeutic formulation demonstrates superior biosafety and a scalable synthesis process, underscoring its translational potential. Collectively, these findings establish OG@HPO as a promising paradigm for overcoming osimertinib resistance by integrating hypoxia modulation with targeted pathway inhibition, bridging a critical gap between preclinical innovation and clinical application.

Materials and Methods

Reagents

Human serum albumin (HSA) was procured from Sigma-Aldrich (USA). Glutathione (GSH) was purchased from Shanghai Macklin Biochemical Technology Co. Ltd (China). Bovine hemoglobin (Hb) was obtained from Hefei Bomei Biotechnology Co. Ltd (China). Osimertinib (OSI) was sourced from MEDCHEMEXPRESS LLC (USA), and Ginsenoside Rg3 (GRg3) was acquired from Shanghai Jinsui Biotechnology Co. Ltd (China). Anhydrous ethanol was supplied by Tianjin Chemical Reagent Co. Ltd (China). The Hypoxyprobe-1 Plus kit was purchased from Hypoxyprobe Inc (USA), the cell hypoxia detection kit was purchased from Shanghai Bestbio Biotechnology Co. Ltd (China), and Hoechst 33342 was obtained from Thermo Fisher Scientific (USA). Phosphate buffer solution (PBS), penicillin-streptomycin, and 0.25% (w/v) trypsin solution were sourced from Beijing Solarbio Science & Technology Co. Ltd (China). RPMI-1640 medium and DMEM high glucose medium were procured from Wuhan Servicebio Technology Co. Ltd (China). Annexin V-FITC/PI Cell Apoptosis Kit was procured from Jiangsu KeyGEN BioTECH Co. Ltd (China).

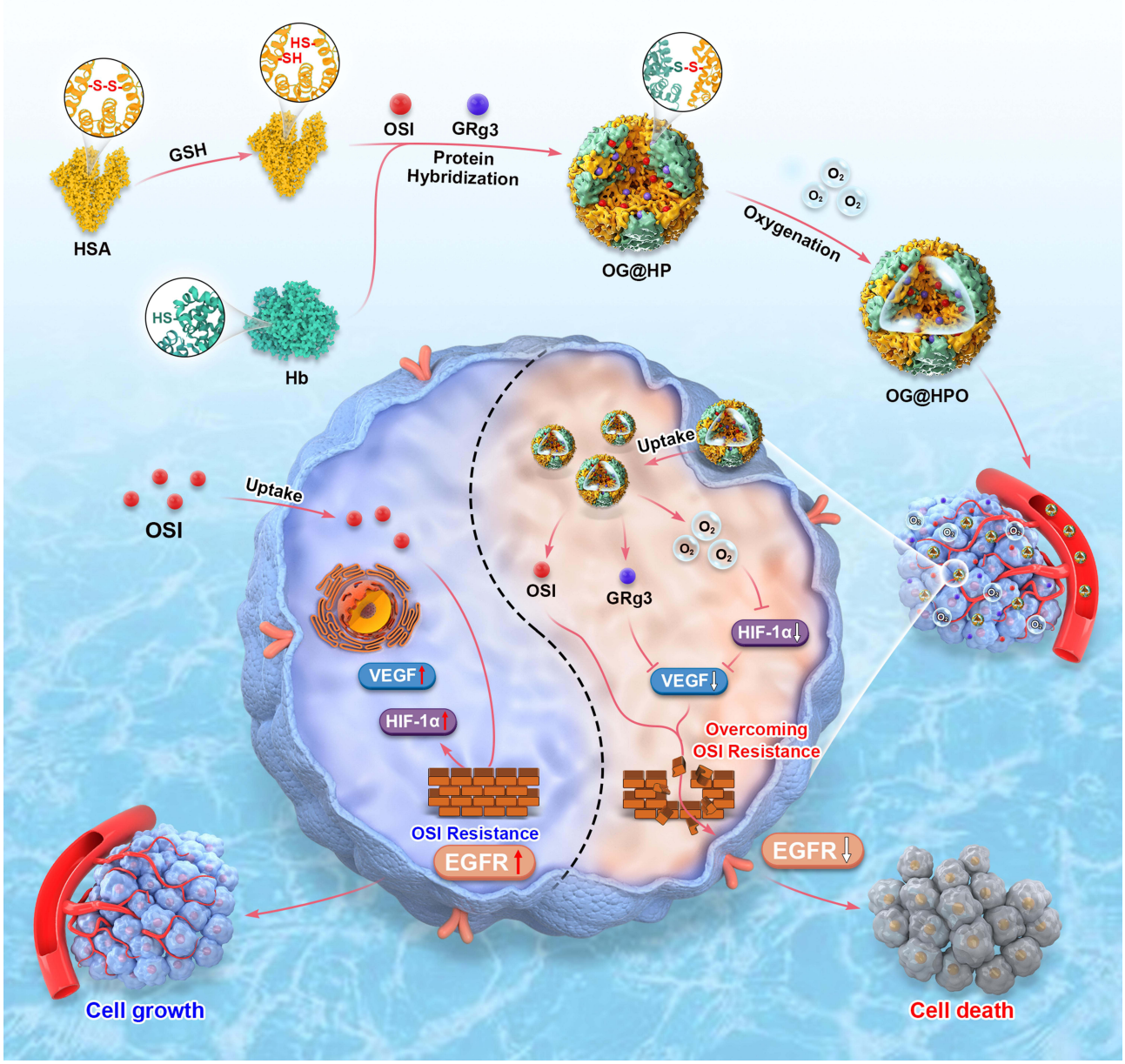

Scheme 1 Preparation of nanomedicine OG@HPO and their application in osimertinib resistant NSCLC targeted therapy.

Human VEGF ELISA kits were purchased from Jiangsu Meimian Industrial Co. Ltd (China). All other chemicals utilized in this study were of analytical reagent grade and were not subjected to further purification. Ultrapure water (18.25 MΩcm, 25°C) was employed for the preparation of all solutions. All chemicals were obtained from commercial sources without further purification.

Cell Lines and Animals

The osimertinib-resistant human lung adenocarcinoma cell line, NCI-H1975/Osimertinib (H1975 OR), was acquired from Zhejiang Meisen Cell Technology Co. Ltd (China). The cells were maintained in a complete medium comprising 10 μM osimertinib, 10% fetal bovine serum (FBS), RPMI 1640 medium, and 1% penicillin/streptomycin (100 U/mL). Human normal lung epithelial cells (BEAS-2B) were obtained from Wuhan Servicebio Technology Co. Ltd (China), and the cells were preserved in a complete medium containing 10% fetal bovine serum (FBS), DMEM high glucose medium and 1% penicillin/streptomycin (100 U/mL). Female BALB/c nude mice were procured from Zhuhai Best Biotechnology

https://doi.org/10.2147/IJN.S531571

Co. Ltd (China), and were housed in a SPF grade barrier environment, maintained at a temperature range of 20–28°C, with a relative humidity of 55% and a 12-hour light/dark cycle. All experimental procedures adhered to the ethical guidelines sanctioned by the Laboratory Animal Center of Guangdong Medical University (GDMU-2024-000035) and complied with the current guidelines and ethical standards approved by the Experimental Animal Centre of Guangdong Medical University.

Synthesis of OG@HPO

Referring to the previously reported method for synthesizing OG@HPO.[33,34] Initially, the preparation of reduced HSA was conducted as follows: 10 mg of HSA was subjected to reduction using GSH (4 mg, 1 mL) for a duration of 1h at room temperature. Subsequently, the resulting solution underwent dialysis (molecular weight cut-off: 3500 Da) for 12h to eliminate excess GSH. Then, 0.05 mg OSI, 0.15 mg GRg3, and 2 mg Hb were incorporated into the reduced HSA solution, ensuring thorough mixing at pH 8.0. To facilitate the precipitation of OG@HPO, 1.5 mL of ethanol solution was introduced into the mixture, which was then subjected to vigorous stirring for 30 min at room temperature to re-establish disulfide bonds. The resulting suspension was purified by performing three cycles of ultrafiltration using an Amicon Ultra-4 centrifugal filter (MW:100 kDa, 4000 rpm) with ultrapure water, effectively removing ethanol, unbound OSI, GRg3, HSA, and Hb, thereby yielding OG@HP nanoparticles. The free OSI and GRg3 in the supernatant were quantified by a UV-Vis spectrophotometer, and the encapsulated efficiency (EE) was calculated using the following formula: EE(%) = (initial dosage weight - free drug weight)/(initial dosage weight) ×100. These OG@HP were subsequently sealed and stored at 4°C. Prior to their utilization in experimental procedures, the OG@HP were exposed to a pure oxygen stream at a flow rate of 2 L/min for 10 min to generate OG@HPO particles, which were then employed in the experiments.

Characterization of OG@HPO

The morphological characteristics of OG@HP were determined using transmission electron microscope (Model H-6009IV, Japan), revealing a typical spherical shape and high monodispersity. The hydrodynamic particle size was assessed with a particle sizer (Nano-ZS90, UK). Ultraviolet-visible spectroscopy was conducted using a ultraviolet spectrophotometer (Shimadzu UV-2450, Japan), identifying characteristic absorption peaks for each component. Fourier transform infrared spectroscopy was used to characterize the absorption peaks and identify the special chemical bonds contained in OG@HPO. Additionally, the oxygen release profiles of OG@HPO were evaluated with a dissolved oxygen analyzer (Mettler Toledo, Switzerland).[35]

In vitro Drug Release Experiments

To evaluate the release of OG@HP, a solution containing OG@HP with 0.2 mg of OSI and 0.2 mg of GRg3 was introduced into GSH solution (10 mM). The system without GSH was identified as control group. This mixture was then placed inside a dialysis membrane with a molecular weight cut-off (MWCO) of 3500 and placed on a constant temperature shaker at 37°C (100 rpm). At various time intervals (0, 1, 2, 4, 6, 8, 10, 24, and 48 h), 1 mL of the dialysate was collected and replaced with 1 mL of PBS. The release rate was determined by analyzing the resulting concentrations using the UV-Vis spectrophotometer.

Cellular Uptake

Cyanine 5.5 (Cy5.5) is used for fluorescent labeling of OG@HP, mix Cy5.5 with OG@HP at room temperature and stir overnight. Confocal laser scanning microscope (CLSM) and flow cytometry were used to assess the ability of the cells to take up OG@HP. Specifically, 3D tumor spheres were formed by inoculating H1975 OR cells at 300 cells per well in U-shaped ultra-low adsorption 96-well plates for 3 days, and then introducing OG@HP at 1, 2, and 4-hour intervals. Subsequently, the cells were washed three times with PBS and incubated with Calcein-AM for 15 minutes to facilitate cell localization. H1975 OR cells were seeded into confocal dishes at a density of 3×10^4 cells per well and incubated overnight. OG@HP was subsequently introduced at time intervals of 1, 2, and 4 h. Following this, the cells were washed 3 times with PBS and incubated with Hoechst 33342 for 10 min to facilitate nuclear localization. Cellular uptake was

then assessed using CLSM, and images were captured. Similarly, H1975 OR cells were seeded at a density of 8×10^4 cells per well in 24-well plates and incubated overnight. OG@HP was added at the same time intervals of 1, 2, and 4 h. Cells were then harvested through digestion and centrifugation, washed 3 times with PBS, and resuspended in PBS. The samples were subsequently analyzed using a flow cytometer (BD FACSAria III, USA).

Cytotoxicity Assays

The cytotoxic effects of OG@HPO on the H1975 OR cell line were evaluated utilizing the CCK-8 assay. H1975 OR cells were seeded into 96-well plates at a density of 8×10^3 cells per well. Following an overnight incubation period, the medium was replaced with a complete medium containing varying concentrations of the test samples. The cells were then incubated for an additional 24 h. Subsequently, the medium was exchanged for one containing CCK-8. Absorbance readings at 450 nm were obtained using a microplate reader (ELISA of PerkinElmer, USA) after the designated incubation period. This procedure was conducted in triplicate for all experimental groups to calculate the mean values. Cell viability and the combination index (CI) were determined using the following equations.

$$Cell\ viability(\%) = \frac{OD_{sample}}{OD_{control}} \times 100\% \tag{1}$$

where OD_{sample} is the OD value in the presence of the sample, and $OD_{control}$ is the OD value of the control group.

$$CI = \frac{IC50(combined\ therapy)}{IC50(OSI\ alone)} + \frac{IC50(combined\ therapy)}{IC50(GRg3\ alone)} \tag{2}$$

where IC50 indicates the semi-inhibited concentration of the preparation. The CI value < 1 indicates synergism, CI value > 1 shows antagonism, and CI value = 1 means additive effects. The calculation was carried out by compusyn software.

Live Cell Staining Assay

The effect of different preparations on H1975 OR cell viability was evaluated utilizing a Calcein-AM/propidium iodide (PI) live/dead cell assay kit. H1975 OR cells were seeded at a density of 8×10^3 cells per well in 96-well plates and incubated overnight at 37°C in an atmosphere containing 5% CO_2. Subsequently, following a 24-hour incubation period with various experimental treatments, the cells were washed with PBS. The cells were then stained with a calcein-AM/PI reagent for 15 min to differentiate between live and dead cells. Images were captured using a live cell imaging system.

Cell Apoptosis Study

Apoptotic cells were identified utilizing the Annexin V-FITC/PI Apoptosis Detection Kit. H1975 OR cells were seeded into 24-well plates at a density of 8×10^4 cells per well and allowed to adhere overnight. The cells were then treated for 24h with PBS, free OSI, O@HP, OG@HP, O@HPO, and OG@HPO, all at an equivalent OSI concentration of 8 μg/mL and a GRg3 concentration of 25 μg/mL. Following treatment, the cells were harvested, washed with PBS, stained with the Annexin V-FITC/PI Apoptosis Detection Kit, and analyzed via flow cytometry.

Tumor Spheres of Live and Dead Cells Staining

The effects of different preparations on the tumor sphere viability of H1975 OR cells were evaluated by using the calcitonin-AM/propidium iodide (PI) live/dead cell assay kit. H1975 OR cells were seeded in U-shaped ultra-low adsorption 96-well plates at a rate of 300 cells per well and incubated at 37 ° C for 3 days in an environment containing 5% CO_2. Subsequently, after 24 hours of treatment with different preparations, the cells were washed with PBS. Then, the cells were stained with calcein-AM/PI reagent for 15 minutes to distinguish between live cells and dead cells. Images were captured using CLSM.

Tumor Spheres of Hypoxia Probe Staining

The effects of different preparations on hypoxia remission of tumor spheres in H1975 OR cells were evaluated using hypoxia probe kits. H1975 OR cells were seeded in U-shaped ultra-low adsorption 96-well plates at a rate of 300 cells per well and incubated at 37 ° C for 3 days in an environment containing 5% CO_2. Subsequently, after 24 hours of treatment with different preparations, the cells were washed with PBS. Then, the cells were stained with $RU(dpp)_3Cl_2$ probe for 30 minutes and incubated with Calcein-AM for 15 minutes to locate the live cells. Images were captured by CLSM.

Western Blot Assay

Following the seeding and overnight incubation of H1975 OR cells in 6-well plates, the cells were cultured with various preparations for a duration of 24 h. Subsequently, the cells underwent digestion, collection, and two rounds of washing before being lysed in RIPA buffer supplemented with protease inhibitors. The protein concentrations of the samples were determined using a BCA protein assay kit. Thereafter, the sample proteins were incubated with antibodies targeting EGFR, phosphorylated EGFR (p-EGFR), HIF-1α, VEGF, and actin. A secondary incubation was performed using a goat anti-rabbit antibody. Images were captured utilizing the CLINX 6100 system and analyzed manually with Servicebio software (AIWBwell TM). The density of protein bands was quantified using ImageJ software, with actin serving as a loading control.

Animal Tumor Models

To develop a tumor xenograft mouse model, a suspension of H1975 OR cells was prepared at a concentration of 1.0×10^7 cells in 100 μL of PBS. This suspension was then used to establish xenografts via subcutaneous injection into the right flank region of 6–8 week-old female BALB/c nude mice.

In vivo Biodistribution Assay

To investigate the in vivo distribution of OG@HPO, H1975 OR tumor-bearing mice with tumor volumes ranging from 200 to 300 mm^3 were randomly assigned to two groups and administered either PBS or OG@HPO. Following the intravenous injection of an equivalent dose of free Cy5.5 and Cy5.5-OG@HPO into the mice via the tail vein, fluorescence imaging was conducted using the IVIS spectroscopy system at 0, 1, 2, 4, 8, 12, and 24 h. After 24 h, the tumors and organs were excised from the mice and subjected to fluorescence analysis to assess tissue distribution.

In vivo Tumor Hypoxia Assays

To assess the hypoxic relief of tumors by OG@HPO, female nude mice bearing H1975 OR tumors were injected tail vein using OG@HP and OG@HPO (1 mg/kg OSI, 3 mg/kg GRg3). After 3 h, mice were given a tail vein injection of pimonidazole hydrochloride (60 mg/kg). Mice were allowed to circulate for 90 min, then euthanized and tumors were collected for frozen sections. Tumor sections were stained with FITC-coupled mouse anti-peramonidazole antibody (dilution 1:200, Hypoxyprobe Inc.) and Alex 488-conjugated goat anti-mouse secondary antibody (dilution 1:200, Jackson Inc).[36]

In vivo Antitumor Efficacy and Mechanisms

When the tumor volumes exceeded 50–100 mm^3, the mice were randomly allocated into six experimental groups, including PBS, free OSI (1 mg/kg OSI), O@HP (1 mg/kg OSI), OG@HP (1 mg/kg OSI, 3 mg/kg GRg3), O@HPO (1 mg/kg OSI and oxygenated), and OG@HPO (1 mg/kg OSI, 3 mg/kg GRg3 and oxygenated). Each group received intravenous injections of the respective formulations (100 μL per mouse) into the tumor-bearing mice. Tumor volume and body weight were monitored every two days over an 18-day period. At the study's conclusion, the mice were humanely euthanized, and the tumors, along with the hearts, livers, spleens, lungs, and kidneys, were excised and fixed in 4% paraformaldehyde solution for subsequent histopathological examination. Blood samples were collected from the mice's eyes for hematological analysis, with the PBS group serving as a control. The blood was centrifuged to separate the serum, and the levels of liver and kidney function indices were quantified using enzyme-linked immunosorbent assay (ELISA).

Statistical Analysis

Statistical analyses were conducted utilizing GraphPad Prism software. Experimental data were expressed as the mean ± standard deviation (SD). All the differences between groups were analyzed using One-way ANOVA. For direct comparison between the two groups, the unpaired *t*-test was used. Statistical significance was determined at the following thresholds: *p < 0.05, **p < 0.01, ***p < 0.001 and ****p < 0.0001, with "ns" indicating no significant difference.

Results and Discussion

Preparation and Characterization of OG@HPO

Hybridized nanoparticles were prepared by a redox-driven assembly process.[33] HSA was first reduced with glutathione to expose free sulfhydryl groups, followed by disulfide bond-mediated hybridization of HSA and Hb to form a stable hybrid protein (HP) matrix.[37] Simultaneous encapsulation of two drugs was achieved during disulfide bond structural reconfiguration, and OSI and GRg3 were integrated into the HP framework to obtain OG@HP. Structural characterization of OG@HP by transmission electron microscope (TEM) revealed monodispersed spherical nanoparticles with an average diameter of 16.4 ± 3.5 nm and good homogeneity (Figure 1a). Dynamic light scattering (DLS) confirmed these findings, showing a hydrodynamic particle size distribution of 64.5 nm for OG@HP, distinct from unmodified HSA (10 nm) and

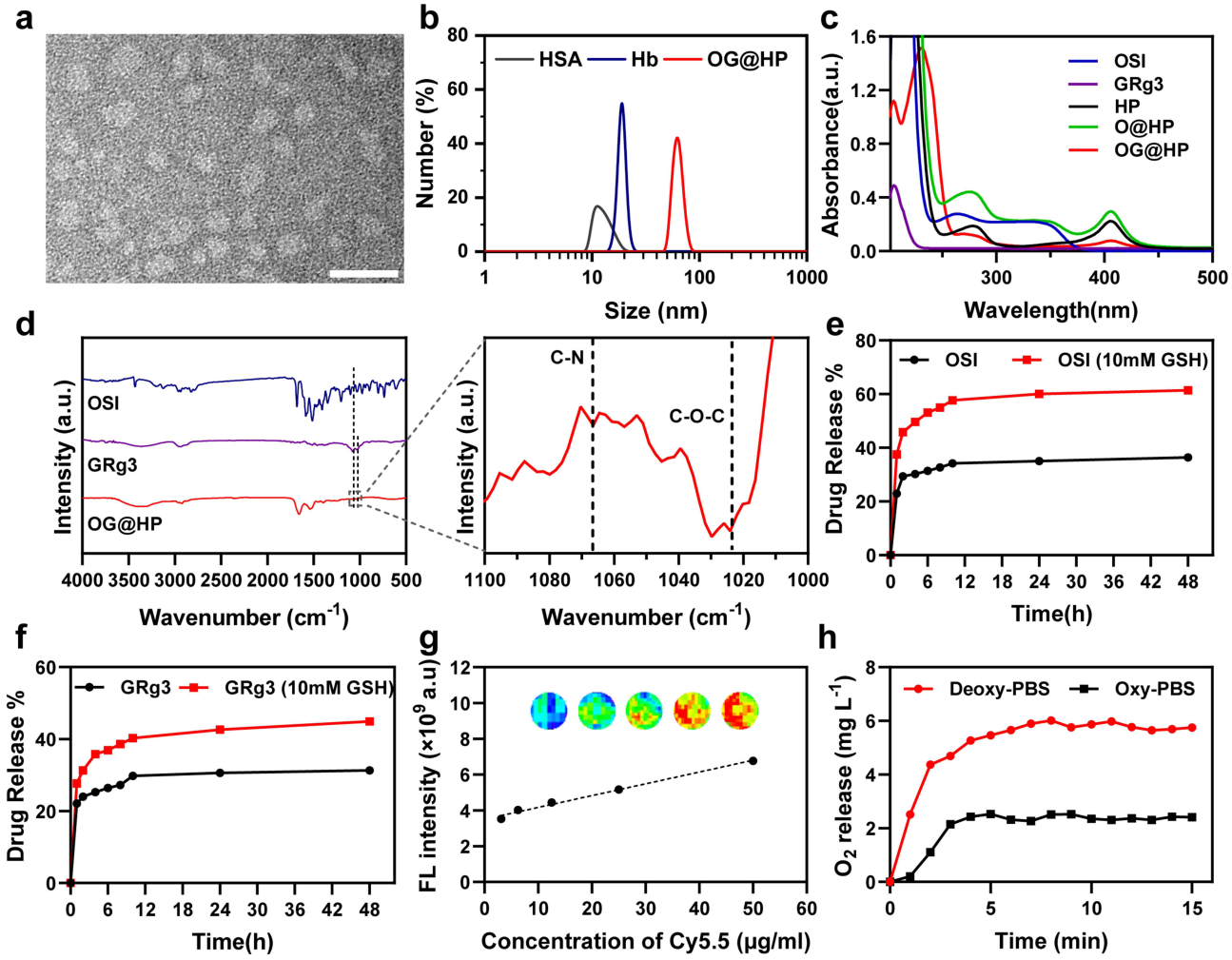

Figure 1 (**a**) TEM image of the OG@HP (scale bar: 50 nm). (**b**) Hydrodynamic diameters of free HSA, Hb, and OG@HP measured by DLS. (**c**) UV–vis absorbance profiles of free OSI, GRg3, and OG@HP. (**d**) FTIR spectra of OSI, GRg3, OG@HP. (**e**) The release curve of OSI in PBS solution and GSH (10 mM). (**f**) The release curve of GRg3 in PBS solution and PBS solution with (10 mM GSH). (**g**) Near-infrared fluorescence (NIRF) intensity and corresponding NIRF images of Cy5.5-OG@HP solution. (**h**) Oxygen release profile of the OG@HPO by estimating the dissolved oxygen in various PBS solutions.

https://doi.org/10.2147/IJN.S531571

Hb (19 nm) (Figure 1b). In addition, it was determined in Figure S1 that the zeta potentials of HSA, Hb and OG@HP were −36.53, −14.27 and −24.37 mV, respectively. The successful construction of OG@HP was confirmed using the characteristic absorption peaks of the UV-visible spectrum, revealing signature absorbance bands at 205 nm, 280 nm, 406 nm, and 334 nm, which confirm successful component integration the specific absorptions of GRg3, HSA, Hb, and OSI, respectively (Figure 1c). Additionally, Fourier transform infrared (FTIR) spectroscopy was used to analyze HSA, Hb, OSI, GRg3 and OG@HP (Figures 1d and S2), identifying OSI's C-N stretching band at 1066 cm^{-1} and GRg3's ether bond stretching band at 1024 cm^{-1}. To quantify the OSI and GRg3 load efficiency in OG@HP, quantitative UV-Vis measurements showed package efficiencies of 64.14% (OSI) and 68.25% (GRg3), validating the payloads of both drugs. These findings confirm the successful synthesis of OG@HP NPs. High levels of GSH exist in the tumor microenvironment. The disulfide bonds in HP respond to the breaking of GSH, leading to the dissociation of nanoparticles and the release of drugs. Therefore, in order to evaluate the release potential of OG@HP responsive GSH, in vitro release kinetics under simulated tumor microenvironment showed that the drug release rate was obvious in the presence of 10 mM GSH, and very low in the absence of GSH (Figure 1e and f). The results showed that OG@HP had excellent drug release ability when triggered by GSH.

The fluorescence signal of Cy5.5 labeled OG@HP in aqueous solution was detected in subsequent studies. The results showed a dose-dependent increase in FL signals ($R^2 = 0.992$), indicating that they support their usefulness in monitoring the real-time distribution of nanomedicines in vivo (Figure 1g). In addition, OG@HPO mediated hypoxia regulation was assessed using a dissolved oxygen analyzer, releasing minimal oxygen in oxygenated PBS solutions and accelerated sustained release in deoxygenated PBS (Figure 1h). The hydrodynamic diameter of OG@HP remained stable without any substantial change in PBS, and RPMI-1640 for 7 days (Figure S3), which indicated its good stability. These results indicate that Hb in OG@HPO is an effective oxygen carrier, and its skilled oxygen carrying and releasing ability is conducive to alleviating tumor hypoxia which provides the possibility for OG@HPO to inhibit HIF-1α/VEGF/EGFR pathway at tumor site and reverse drug resistance.

In vitro Antitumor Activity of OG@HPO

Due to the hypoxia, high GSH levels and the targeting characteristics of HSA in the tumor microenvironment, OG@HPO can be efficiently transported to the target site for efficient accumulation and cellular uptake. To confirm the targeted delivery capability of nanomedical drugs, we evaluated the targeting capability of Cy5.5-labeled OG@HP on H1975 OR cells utilizing CLSM. Time-dependent red fluorescence intensification revealed progressive nanoparticle internalization (Figure S4). Semi-quantitative analysis showed that the fluorescence intensity at 4 h was significantly higher than that at 1,2 h (Figure S5). Meanwhile, the uptake of 3D tumor spheres of H1975 OR cells was evaluated, and the results showed that red fluorescence accumulated within the tumor spheres over time (Figures 2a and S6). Subsequently, we validated the CLSM results using flow cytometry to quantify time-dependent cell uptake (Figure 2b). The results showed a significant increase of OG@HP in the cells over time, which is consistent with the CLSM results. Collectively, the time-dependent increase in fluorescence intensity indicates efficient cellular internalization of OG@HPO, which is critical for enhancing drug accumulation in resistant tumor cells and overcoming efflux-mediated resistance.

To assess the potential toxicity of OG@HPO on H1975 OR cells, we used CCK-8 assay to evaluate the impact of varying concentrations of OG@HP on cell viability following a 24-hour incubation period. The findings indicated that low concentrations of OG@HP exhibited minimal or no cytotoxicity towards the cells. However, when the OSI concentration reached 4 μg/mL and the GRg3 concentration reached 12.5 μg/mL, a slight toxicity was observed, with cell viability exceeding 80%. At increased concentrations, specifically 32 μg/mL for OSI and 100 μg/mL for GRg3, cell viability decreased to approximately 50% (Figure S7). These data confirm that only high concentrations of OG@HP induce significant cytotoxic effects. Therefore, we also analyzed the synergy effect of the data and obtained CI=0.804, confirming that the combination of the two drugs improved the therapeutic effect. To further investigate the biocompatibility of nanocarriers, the cck8 experiment of nanocarriers (HP) was conducted on normal lung epithelial BEA-2B cells and lung cancer H1975 OR cells. The results showed that the cell viability of both groups remained above 95%, verifying the in vitro biological safety of the nanocarriers (Figure S8). In addition, we went on to compare the cytotoxicity of the same dose of different formulations at 24 h incubation (8 μg/mL for OSI and 25 μg/mL for GRg3) and and found that

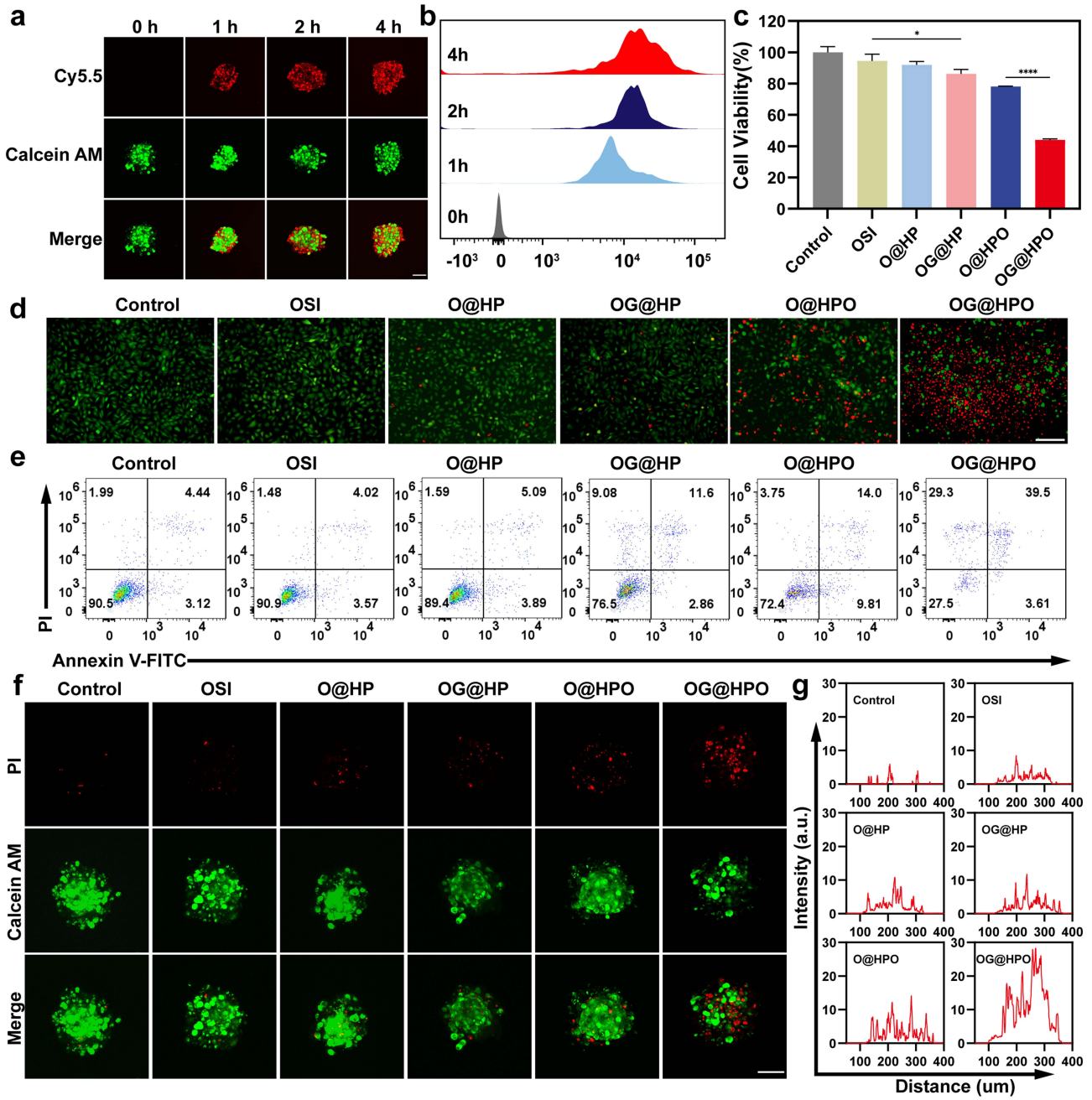

Figure 2 (**a**) CLSM images of tumor sphere models of H1975 OR cells incubated at OG@HP for different durations (scale bar: 100 μm). (**b**) Using OG @ HP H1975 OR cells after different incubation time of intake flow cytometry analysis. (**c**) Toxic effects of different formulation treatments on H1975 OR cells (n=3 independent experiments, significant differences were defined as *p < 0.05, and ****p < 0.0001). (**d**) FL images of H1975 OR cells after calcein-AM and PI staining under different treatment methods (scale bar: 20 μm). (**e**) Flow cytometry analysis of H1975 OR cell apoptosis. (**f**) CLSM images of the 3D tumor sphere model of H1975 OR after treatment with different preparations and staining with live and dead cells (green: live cells; red: dead cells; scale bar: 100 μm). (**g**) Semi-quantitative analysis of the PI (red) fluorescence in (f) was conducted using ImageJ.

OSI loaded into the nanocarrier achieved O@HP, with a survival rate of 92%. This might be due to the targeted delivery of the nanocarrier increasing the accumulation of OSI in tumor cells. When OSI and GRg3 are simultaneously loaded into nanometers, OG@HP is obtained, and the survival rate drops to 86.28%; Oxygenation treatment of O@HP (ie O@HPO) had a survival rate of 78.07%, which might be due to the relief of hypoxia in the tumor microenvironment and the inhibition of HIF-1α, which increased the sensitivity of tumor cells to osimertinib; Oxygenation of OG@HP yields OG@HPO, which has a better tumor suppressive effect compared with the other groups (survival rate: 44.06%)

https://doi.org/10.2147/IJN.S531571

(Figure 2c). To further verify the cytotoxic effects of OG@HPO, we fluorescently stained live/dead cells using membrane permeable Calcein-AM (green fluorescence) and PI (red fluorescence). Fluorescence imaging showed that the PBS and OSI groups mainly showed green signals, while the H1975 OR cells treated with OG@HPO showed a large number of red PI positive cells (Figure 2d). Semi-quantitative analysis of the red fluorescence representing dead cells in Figure 2d revealed that the red fluorescence in the OG@HPO group was as high as 64% (Figure S9). The results showed that OSI alone had limited ability to damage cells, but with the aid of GRg3 and oxygen-carrying Hb, OSI would produce a satisfying effect. Notably, the therapeutic effect of the nano platform is superior to that of monotherapy.

Annexin V-FITC/PI double staining for quantitative apoptosis analysis showed that OG@HPO induced apoptosis in 50.7% of H1975 OR cells, 6.3 times that in the control group (8.01%) and the free OSI group (8.10%) (Figure 2e). Quantitative analysis of Figure 2e showed that OG@HPO (46.07%) induced 6.4 times more cell death than the Control group (7.24%) (Figure S10). To better verify the efficacy of OG@HPO on drug-resistant lung cancer, the 3D spherical model of H1975 OR cells was treated differently. After 24 hours, Calcein-AM (green) was used to label live cells and PI (red) to label dead cells (Figure 2f). Strong green fluorescence was observed in the control group, with only a small amount of red fluorescence on the outer layer. In the OG@HPO group, the intensity of green fluorescence decreased, and the red fluorescence diffused from the core to the outer layer, indicating that the nanoparticles could penetrate the tumor spheres and induce deep cell death. Semi-quantitative analysis showed that the tumor spheres in the OG@HPO group all had red fluorescence, especially in the core layer (200–300 μm depth), the intensity of red fluorescence was significantly enhanced, indicating that the drug achieved efficient killing by enhancing penetration (Figure 2g). This synergistic apoptosis induction highlights the therapeutic advantage of concurrent VEGF inhibition and hypoxia alleviation.

In vitro Improvement of Hypoxia and HIF-1α/VEGF/EGFR Inhibition

Herein, $RU(dpp)_3Cl_2$ probe was used to detect the hypoxia-improving effect of OG@HPO on H1975 OR tumor spheres. After 24 hours of treatment with different preparations on the tumor spheres, it could be observed that the red fluorescence of O@HPO and OG@HPO was significantly lower than that of the control group, and due to the better therapeutic effect of OG@HPO, the volume of the tumor spheres was significantly smaller than that of the other groups (Figure 3a). Semi-quantitative analysis showed that the hypoxia fluorescence intensity in the OG@HPO group was significantly reduced, especially at 200 μm. These results indicate that this nanomedicine is an excellent oxygen supply agent and can significantly improve the hypoxic microenvironment of tumor spheres (Figure 3b). Previous studies have shown that abnormal activation of EGFR contributes to drug resistance in tumor cells.[38] We analyzed OG@HP inhibition of drug-resistance related biomarkers by Western blotting. After incubation with various drugs for 24 h, there was little difference between the control, free OSI, and O@HP (contains OSI) groups. On the contrary, O@HPO (consists of OSI and oxygenated) and OG@HPO groups showed down-regulation of HIF-1α, while OG@HP (consists of OSI and GRg3), O@HPO, and OG@HPO groups showed decreased expression of EGFR, p-EGFR, and VEGF proteins (Figure 3c–g). Meanwhile, ELISA confirmed the decreased VEGF secretion level in the supernatant of H1975 OR cell culture treated with OG@HPO (Figure 3h). These results suggest that the nano platform works through oxygen-mediated HIF-1α down-regulation in conjunction with GRg3-driven vascular endothelial growth factor/epidermal growth factor receptor axis inhibition, which significantly improves the sensitivity of osimertinib and effectively reverses acquired resistance.

In vivo Biodistribution of OG@HPO

HSA is widely popular for its excellent biocompatibility and non-toxicity. It can bind to the GP60 receptor on the cell surface, effectively enriching drugs in the body.[39] At the same time, it enhances the accumulation of drugs in the body through high permeability and retention effect (EPR effect).[40,41] The hypoxia relief and GSH response release characteristics of OG@HPO, combined with the targeting performance of albumin, further enhance its ability to target tumors in vivo and the enrichment of nanomedicines at tumor sites.

Prior to in vivo therapeutic experiments, we performed a biological distribution analysis of OG@HPO targeting in a tumor mouse model. The fluorescence distribution in mice within 24h was monitored by intravenous injection of Cy5.5 labeled OG@HPO (Cy5.5-OG@HPO) (Figure 4a). Fluorescence tracking showed that the fluorescence signal of the free dye group at the tumor site was first increased, and then the fluorescence was quickly cleared. In contrast, after 24h, the

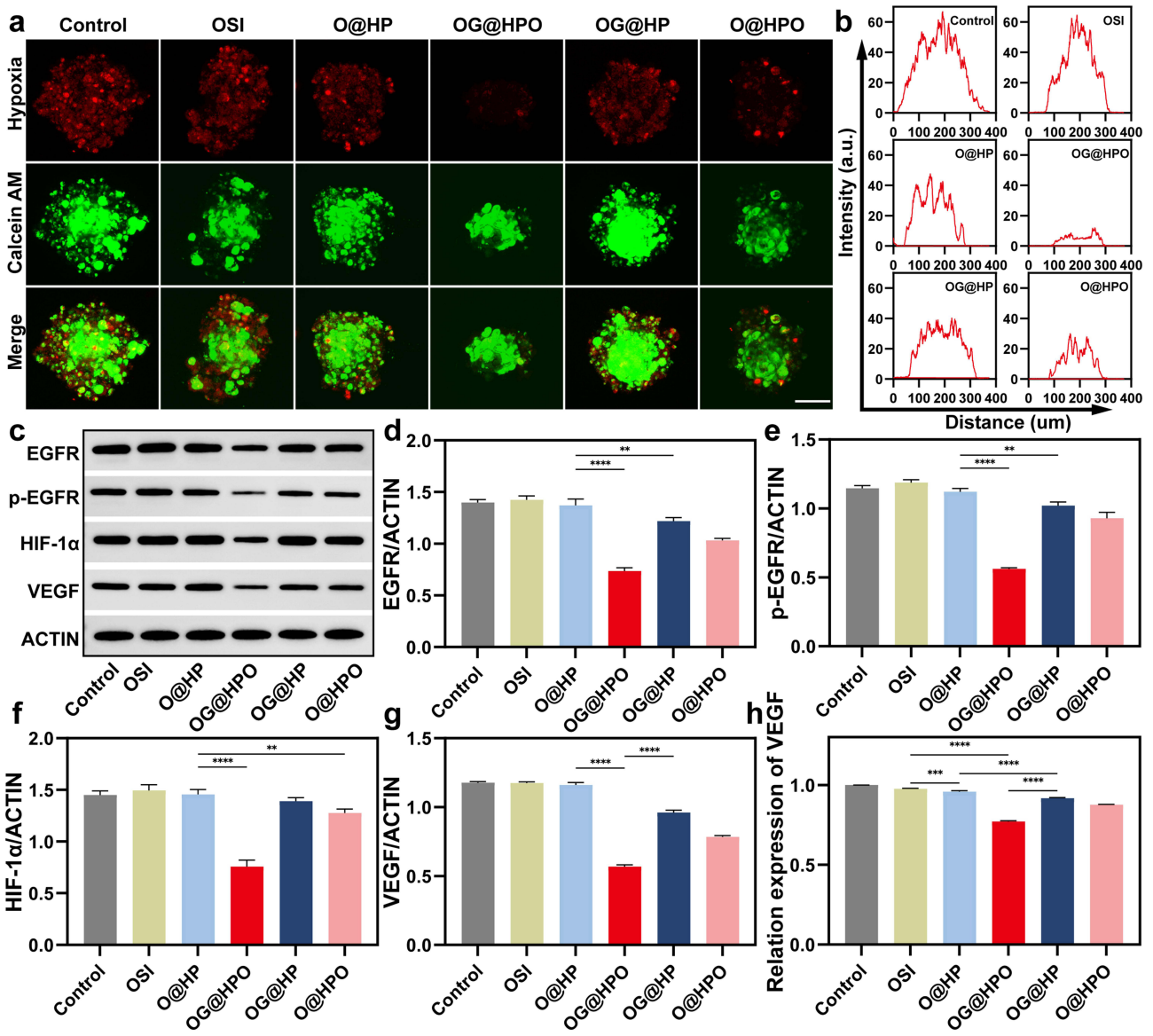

Figure 3 (**a**) The hypoxia fluorescence of 3D tumor spheres of H1975 OR after different treatments was captured by confocal microscopy (red: hypoxia signal; green: living cells; scale bar: 100 μm). (**b**) Semi-quantitative analysis was conducted on the hypoxia fluorescence (red) in (a). (**c**) The expression of EGFR, p-EGFR, HIF-1α and VEGF with different agents was detected by immunoblotting. (**d**) EGFR, (**e**) p-EGFR, (**f**) HIF-1α and (**g**) VEGF are semi-quantitative analysis of the grey values of the bands for (c). (**h**) Determination of VEGF levels in supernatants of H1975 OR cells treated with different preparations by ELISA analysis. Significant differences were defined as $^{**}p < 0.01$, $^{***}p < 0.001$, and $^{****}p < 0.0001$.

fluorescence of the Cy5.5-OG@HPO group was sustained. It is clear from the mean fluorescence intensity analysis that the administered group had higher fluorescence intensity at all time intervals compared to the control free Cy5.5. In particular, there was a sharp contrast after 4h, when the mean fluorescence intensity of Cy5.5-OG@HPO group reached 8.16×10^3, while that of free Cy5.5 was 4.86×10^3, which again demonstrated that OG@HPO NPs could target and accumulate in tumors (Figure 4b). Finally, major organs and tumours were excised 24h after injection and fluorescence intensity was measured. The results showed weaker fluorescence signals in the heart, spleen and kidney in the Cy5.5-OG@HPO group, indicating that the OG@HPO were less toxic to these three organs and had a certain degree of biosafety (Figure 4c). Analysis of in vivo and in vitro organs 24h after administration showed that OG@HPO was preferentially accumulated in tumors, with limited accumulation in liver and kidney (Figure 4d). In summary, OG@HPO can effectively target tumors and prolong the action time of drugs, improve the efficacy of the nanosystem in vivo, and the system has good biocompatibility, so as to minimize adverse reactions. In addition, in vivo fluorescence staining was

https://doi.org/10.2147/IJN.S531571

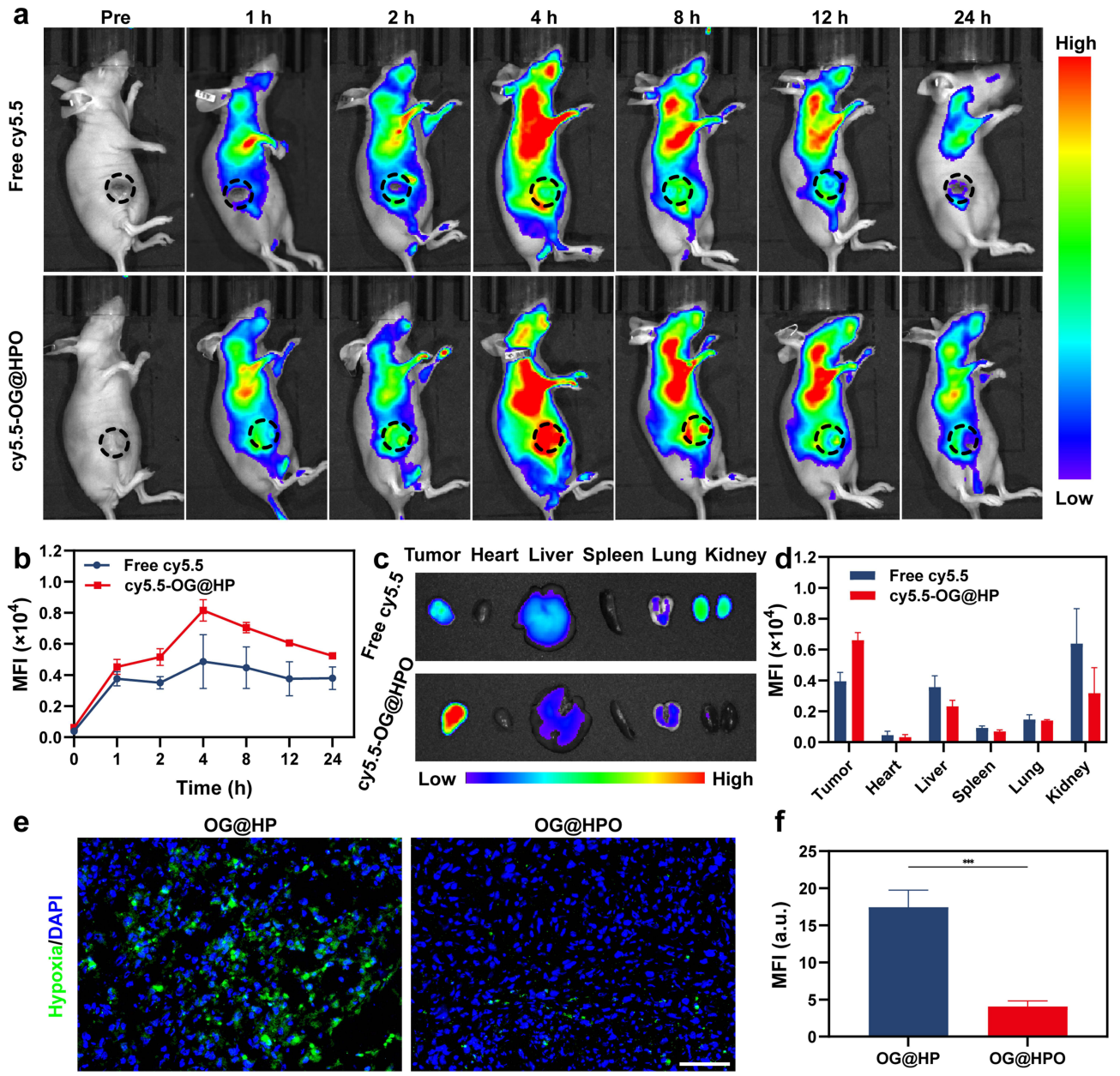

Figure 4 (**a**) Injection of free Cy5.5 and Cy5.5-OG@HPO different time points after the mice in vivo fluorescence imaging (The black dashed circle shows the tumor area). (**b**) Different time points average quantitative analysis of the fluorescence intensity of tumor site (n = 3). (**c**) Fluorescence imaging of tumors and major organs 24 h after Cy5.5 and Cy5.5-OG@HPO injection. (**d**) The average fluorescence intensity of tumors and major organs in each group was quantitatively analyzed (n = 3). (**e**) Representative tumor hypoxia immunofluorescence staining of tumor sections from mice treated with injections of OG@HP and OG@HPO. Blue and green colours represent nuclei and hypoxia-positive regions, respectively (scale bar: 100 μm). (**f**) A semi-quantitative analysis was performed on the hypoxic-positive area (Significant differences were defined as ***$p < 0.001$).

performed using pimonidazole hydrochloride as a tumour hypoxia probe, which forms covalent bonds with cellular macromolecules in hypoxic environments, followed by immunofluorescence detection of pimonidazole hydrochloride-protein adducts to evaluate OG@HPO alleviate the effect of tumor hypoxia.[42] The results showed that the tumor sections of mice in the OG@HP group showed obvious green fluorescence signal, while the green fluorescence signal of the OG@HPO group was significantly reduced, indicating that oxygen regulation could effectively reduce the anoxic area of tumor microenvironment (Figure 4e). Subsequently, a semi-quantitative analysis of Figure 4e showed that the anoxic positive signal in the OG@HPO group was much higher than that in the OG@HP group (Figure 4f). In a word, OG@HPO can effectively relieve tumor hypoxia.

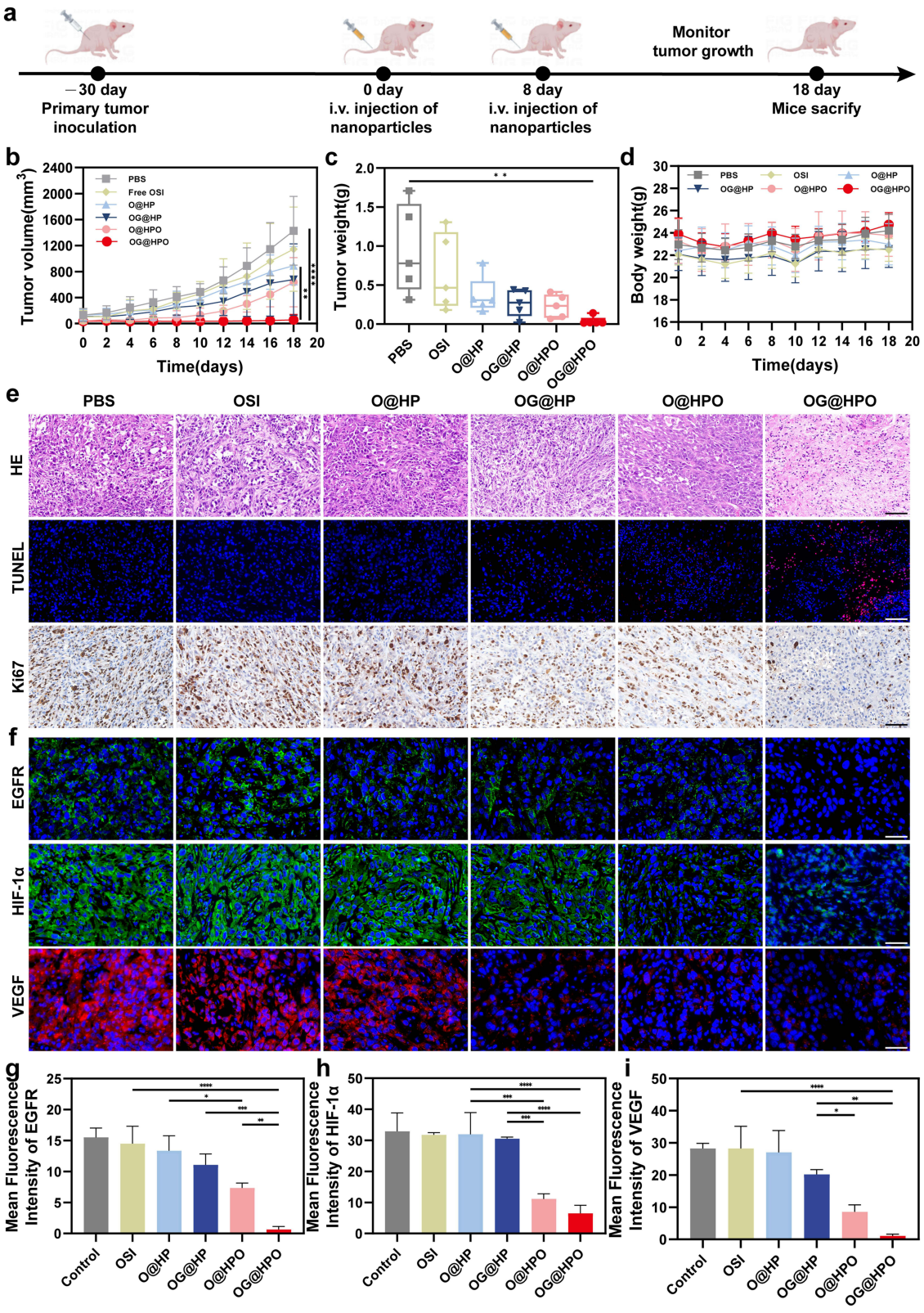

Figure 5 (**a**) Schedule of tumours treated with OG@HPO. (**b**) Changes in tumour volume over 18 days of treatment in different dose groups (Significant differences were defined as **p < 0.01 and ****p < 0.0001, n=5). (**c**) Tumour weights after 18 days of treatment in different dose groups (Significant differences were defined as **p < 0.01, n=5). (**d**) Average body weight of mice in different treatment groups within 18 days after treatment (n=5). (**e**) Histological analyses of tumours in different dose groups, including H&E, Ki67, and TUNEL (Scale bar: 100 μm). (**f**) Immunofluorescence images of EGFR (green), HIF-1α (green), and VEGF (red) staining in the tumour sections of different groups. Nucleus stained with DAPI (blue). (Scale bar: 50 μm). (**g–i**) Immunofluorescence semi-quantification of EGFR (green), HIF-1α (green), and VEGF (red) corresponding to (**f**), respectively. (Significant differences were defined as *p < 0.05, **p < 0.01, ***p < 0.001, and ****p < 0.0001).

https://doi.org/10.2147/IJN.S531571

In vivo Antitumor Efficacy of OG@HPO

The therapeutic potential of OG@HPO in vivo was evaluated in a BALB/c nude mouse xenograft model established by subcutaneous injection of 1×10^7 H1975 OR cells (osimertinib resistant NSCLC strain) into the upper right leg. As shown in Figure 5a, when the tumor volume of the mouse model reached about 100 mm^3, the animals were randomly divided into 6 treatment groups (n = 4) for comparison and analysis, and 100 μL preparations were injected through the tail vein on day 0 and day 8, respectively, including: (1) PBS, (2) OSI, (3) O@HP, (4) OG@HP, (5) O@HPO and (6) OG@HPO. OSI is administered at a dose of 1 mg/kg and GRg3 is administered at a dose of 3 mg/kg. Tumor volume and body weight of the animals were monitored for 18 days after administration. As shown in the tumor growth curve, the OG@HPO group showed the most effective tumor inhibition, while the OG@HP and O@HPO groups showed limited tumor inhibition, demonstrating the efficacy of combined enhancement of osimertinib (Figure 5b). After the experiment, the tumors of the animals were collected, photographed and weighed (Figures 5c and S11), and the results were consistent with the tumor growth curve. These results suggest that OG@HPO can effectively target delivery and relieve hypoxia in vivo, while exhibiting significant combined antitumor efficacy in conjunction with VEGF inhibitors. The body weight of the 6 groups of mice did not fluctuate significantly throughout the course of treatment (Figure 5d), indicating the biosafety of OG@HPO in vivo. Histopathological analysis showed that the major organs stained with Hematoxylin and Eosin (H&E) had normal morphology, and the blood test results of liver and kidney indexes were all within the physiological range, which further confirmed the good biocompatibility of OG@HPO in vivo (Figure S12).

To further validate the anti-tumor efficacy of OG@HPO, a comprehensive analysis was conducted following an 18-day treatment period. At the conclusion of this monitoring phase, euthanasia in mice, and the removal of tumor and the main organs and collect carefully for subsequent histological examination. The findings, presented in Figure 5e, were derived from H&E, TUNEL, and Ki-67 staining techniques, which revealed differential levels of tumor damage across the various treatment groups. This was characterized by cellular atrophy, nuclear chromatin condensation, and fragmentation. Notably, in the OG@HPO treatment group, H1975 OR cells exhibited a higher number of apoptotic or necrotic cells and a reduced number of proliferating cells. These observations underscore the superior anti-tumor efficacy of OG@HPO.

In vivo Antitumor Mechanism Analysis of OG@HPO

Previous studies have shown that OG@HPO multiple inhibition of HIF-1α/VEGF/EGFR axis improves tumor sensitivity and reverses osimertinib resistance. Therefore, we quantitatively assessed the in vivo tumor expression profiles of these three targets in the treatment cohort using immunofluorescence analysis. As shown in Figure 5f–i, the differences between PBS group and OG@HPO group were statistically significant. Specifically, the expression of EGFR, HIF-1α and VEGF was significantly decreased in the OG@HPO group compared with the PBS group. There was no significant difference in HIF-1α expression between treatment groups in the free OSI, O@HP, and OG@HP groups, possibly because hypoxia response was not improved after these treatments. On the contrary, the expression of HIF-1α in tumor tissues treated with O@HPO and OG@HPO was significantly decreased, indicating that oxygen regulation of HIF-1α was effectively down-regulated. There were significant differences in the expression of EGFR and VEGF between the OG@HPO group and the OG@HP group, which could be attributed to the combined effect of GRg3 inhibition of VEGF and oxygen enhancement to decrease EGFR expression. These findings are consistent with Western blot at the cellular level, confirming that the OG@HPO triple strategy is effective in down-regulating EGFR, demonstrating a synergistic effect in osimertinib-resistant NSCLC.

Limitations and Future Directions

This study presents an innovative nanomedicine capable of reversing tumor resistance and fighting tumors via the HIF-1α/VEGF/EGFR pathway. However, the current study still has limitations. On the one hand, in vivo efficacy and tumor recurrence are issues that need to be monitored over time. This would help to achieve a comprehensive assessment of the antitumor efficacy of OG@HPO and would be a strong evidence for its clinical translation. On the other hand, the selection of tumor models needs to be further improved. The currently selected mice (female BALB/c nude mice) have weaker immune functions and differ greatly from clinical tumor models. It does not respond well to the immune response at the tumor site. This may ignore the interaction between OG@HPO and the immune system and hinder the study of its mechanism of action. Based on these shortcomings, future research directions should be optimized. Long-term

monitoring of tumors in in vivo experiments should be initially achieved to lay the foundation for clinical translation. The use of immune-activated mouse models to explore the role of anti-tumor immune response will provide a more reliable basis for the mechanism of drug resistance reversal. The resolution of these limitations will further inspire the potential application of nanomedicines in the direction of reversing tumor drug resistance.

Conclusion

A hybrid protein-oxygen nanocarrier (OG@HPO) is proposed that encapsulate osimertinib and ginsenoside Rg3 in nanosystems for precision therapy of osimertinib-resistant NSCLC. The nanocarrier-mediated active targeting realizes precise co-delivery of EGFR-TKI, VEGF inhibitors and molecular oxygen to tumors, in response to hypoxia and GSH release in the tumor microenvironment, tumor oxygenation is achieved, and hypoxia-induced VEGF/EGFR pathway is doubly destroyed, so as to improve tumor sensitivity to osimertinib and achieve the ultimate goal of reversing osimertinib resistance. This study pioneered a platform to simultaneously target cancer drivers and hypoxia, linking tumor microenvironment regulation with precision molecular interventions and providing a blueprint for the next generation of combination therapies in precision oncology. However, translating OG@HPO into clinical application requires considering the effectiveness of the immunoactive osimertinib resistance model to better simulate human tumor-immune interactions and to validate it in patient-derived xenograft models. By addressing these challenges, OG@HPO is expected to advance from the laboratory to clinical practice, providing a new strategy for overcoming osimertinib resistance in non-small cell lung cancer.

Acknowledgments

This work was supported by Natural Science Foundation of Guangdong Province (2024A1515030063), Dongguan Social Development Science and Technology Project (20221800906342), Beijing Kangmeng Charity Foundation Medical Research Development Fund Project, Clinical and Basic Research Special Program (TB219009), Discipline Construction Project of Guangdong Medical University (4SG24015G), Construction Project of Nano Technology and Application Engineering Research Center of Guangdong Medical University (4SG24179G) and Funds for PHD researchers of Guangdong Medical University in 2024.

Disclosure

The authors report no conflicts of interest in this work.

References

1. Bray F, Laversanne M, Sung H, et al. Global cancer statistics 2022: GLOBOCAN estimates of incidence and mortality worldwide for 36 cancers in 185 countries. CA. *Cancer J Clin*. 2024;74(3):229–263. doi:10.3322/caac.21834
2. A TA, Solomon BJ, Sequist LV, et al. Lung cancer. *Lancet*. 2021;398(10299):535–554. doi:10.1016/S0140-6736(21)00312-3
3. Harrison PT, Vyse S, Huang PH. Rare epidermal growth factor receptor (EGFR) mutations in non-small cell lung cancer. *Semin Cancer Biol*. 2020;61:167–179. doi:10.1016/j.semcancer.2019.09.015
4. Rosell R, Moran T, Queralt C, et al. Screening for epidermal growth factor receptor mutations in lung cancer. *N Engl J Med*. 2009;361 (10):958–967. doi:10.1056/NEJMoa0904554
5. Gazdar AF. Activating and resistance mutations of EGFR in non-small-cell lung cancer: role in clinical response to EGFR tyrosine kinase inhibitors. *Oncogene*. 2009;28(Suppl 1):S24–S31. doi:10.1038/onc.2009.198
6. Vyse S, Huang PH. Targeting EGFR exon 20 insertion mutations in non-small cell lung cancer. *Signal Transduct Target Ther*. 2019;4:5. doi:10.1038/s41392-019-0038-9
7. Fu K, Xie F, Wang F, et al. Therapeutic strategies for EGFR-mutated non-small cell lung cancer patients with osimertinib resistance. *J Hematol Oncol*. 2022;15(1):173. doi:10.1186/s13045-022-01391-4
8. Voelker R. Adjuvant therapy approved for NSCLC. *JAMA*. 2021;325(5):426 doi:10.1001/jama.2021.0168.
9. Fillon M. Osimertinib prolongs progression-free lung cancer survival after chemotherapy. *CA Cancer J Clin*. 2024;74(5):402–404. doi:10.3322/caac.21862
10. Kim TH, Choi JH, Ahn MS, et al. Differential efficacy of tyrosine kinase inhibitors according to the types of EGFR mutations and agents in non-small cell lung cancer: a real-world study. *BMC Cancer*. 2024;24(1):70. doi:10.1186/s12885-023-11782-6
11. Wu YL, Tsuboi M, He J, et al. Osimertinib in resected EGFR-mutated non-small-cell lung cancer. *N Engl J Med*. 2020;383(18):1711–1723. doi:10.1056/NEJMoa2027071
12. Ramalingam SS, Vansteenkiste J, Planchard D, et al. Overall survival with osimertinib in untreated, EGFR-mutated advanced NSCLC. *N Engl J Med*. 2020;382(1):41–50. doi:10.1056/NEJMoa1913662
13. Chmielecki J, Gray JE, Cheng Y, et al. Candidate mechanisms of acquired resistance to first-line osimertinib in EGFR-mutated advanced non-small cell lung cancer. *Nat Commun*. 2023;14(1):1070. doi:10.1038/s41467-023-35961-y

14. Zhou F, Guo H, Xia Y, et al. The changing treatment landscape of EGFR-mutant non-small-cell lung cancer. *Nat Rev Clin Oncol*. 2025;22(2):95–116. doi:10.1038/s41571-024-00971-2
15. de Scordilli M, Michelotti A, Bertoli E, et al. Targeted therapy and immunotherapy in early-stage non-small cell lung cancer: current evidence and ongoing trials. *Int J Mol Sci*. 2022;23(13):7222. doi:10.3390/ijms23137222
16. Chaft JE, Rimner A, Weder W, et al. Evolution of systemic therapy for stages I-III non-metastatic non-small-cell lung cancer. *Nat Rev Clin Oncol*. 2021;18(9):547–557. doi:10.1038/s41571-021-00501-4
17. Miyauchi E, Morita S, Nakamura A, et al. Updated analysis of NEJ009: gefitinib-alone versus gefitinib plus chemotherapy for non-small-cell lung cancer with mutated EGFR. *J Clin Oncol*. 2022;40(31):3587–3592. doi:10.1200/JCO.21.02911
18. Noronha V, Patil VM, Joshi A, et al. Gefitinib versus gefitinib plus pemetrexed and carboplatin chemotherapy in EGFR-mutated lung cancer. *J Clin Oncol*. 2020;38(2):124–136. doi:10.1200/JCO.19.01154
19. Kibirova A, Mattes MD, Smolkin M, et al. The journey of an EGFR-mutant lung adenocarcinoma through erlotinib, osimertinib and ABCP immunotherapy regimens: sensitivity and resistance. *Case Rep Oncol*. 2019;12(3):765–776. doi:10.1159/000503417
20. Lisberg A, Cummings A, Goldman JW, et al. A phase II study of pembrolizumab in EGFR-mutant, PD-L1+, tyrosine kinase inhibitor naïve patients with advanced NSCLC. *J Thorac Oncol*. 2018;13(8):1138–1145. doi:10.1016/j.jtho.2018.03.035
21. Wang X, Wang F, Zhong M, et al. The biomarkers of hyperprogressive disease in PD-1/PD-L1 blockage therapy. *Mol Cancer*. 2020;19(1):81. doi:10.1186/s12943-020-01200-x
22. Liu GH, Chen T, Zhang X, et al. Small molecule inhibitors targeting the cancers. *MedComm*. 2022;3(4):e181. doi:10.1002/mco2.181
23. Passaro A, Jänne PA, Mok T, et al. Overcoming therapy resistance in EGFR-mutant lung cancer. *Nat Cancer*. 2021;2(4):377–391. doi:10.1038/s43018-021-00195-8
24. Liao YY, Tsai CL, Huang HP. Optimizing osimertinib for NSCLC: targeting resistance and exploring combination therapeutics. *Cancers*. 2025;17(3):459. doi:10.3390/cancers17030459
25. Thangavelu L, Imran M, Alsharari SH, et al. Exploring hypoxia-induced ncRNAs as biomarkers and therapeutic targets in lung cancer. *Pathol Res Pract*. 2024;263:155613. doi:10.1016/j.prp.2024.155613
26. Nilsson MB, Robichaux J, Herynk MH, et al. Altered regulation of HIF-1α in naive- and drug-resistant EGFR-mutant NSCLC: implications for a vascular endothelial growth factor-dependent phenotype. *J Thorac Oncol*. 2021;16(3):439–451. doi:10.1016/j.jtho.2020.11.022
27. Jin Q, Huang F, Xu X, et al. High expression of hypoxia inducible factor 1α related with acquired resistant to EGFR tyrosine kinase inhibitors in NSCLC. *Sci Rep*. 2021;11(1):1199. doi:10.1038/s41598-020-79801-1
28. Tao Y, Jakobsson V, Chen X, et al. Exploiting albumin as a versatile carrier for cancer theranostics. *Acc Chem Res*. 2023;56(18):2403–2415. doi:10.1021/acs.accounts.3c00309
29. Zhang N, Mei K, Guan P, et al. Protein-based artificial nanosystems in cancer therapy. *Small*. 2020;16(23):e1907256. doi:10.1002/smll.201907256
30. Ye Q, Zheng D, Chen K, et al. Research progress in oxygen carrier design and application. *Mol Pharm*. 2023;20(9):4373–4386. doi:10.1021/acs.molpharmaceut.3c00289
31. Infantino V, Santarsiero A, Convertini P, et al. Cancer cell metabolism in hypoxia: role of HIF-1 as key regulator and therapeutic target. *Int J Mol Sci*. 2021;22(11):5703. doi:10.3390/ijms22115703
32. Liu TG, Huang Y, Cui DD, et al. Inhibitory effect of ginsenoside Rg3 combined with gemcitabine on angiogenesis and growth of lung cancer in mice. *BMC Cancer*. 2009;9:250. doi:10.1186/1471-2407-9-250
33. Luo Z, Tian H, Liu L, et al. Tumor-targeted hybrid protein oxygen carrier to simultaneously enhance hypoxia-dampened chemotherapy and photodynamic therapy at a single dose. *Theranostics*. 2018;8(13):3584–3596. doi:10.7150/thno.25409
34. Chen Z, Liu L, Liang R, et al. Bioinspired hybrid protein oxygen nanocarrier amplified photodynamic therapy for eliciting anti-tumor immunity and abscopal effect. *ACS Nano*. 2018;12(8):8633–8645. doi:10.1021/acsnano.8b04371
35. Yin T, Yin J, Ran H, et al. Hypoxia-alleviated sonodynamic therapy based on a hybrid protein oxygen carrier to enhance tumor inhibition. *Biomater Sci*. 2021;10(1):294–305. doi:10.1039/D1BM01710A
36. Wu SY, Ye YX, Zhang Q, et al. Multifunctional protein hybrid nanoplatform for synergetic photodynamic-chemotherapy of malignant carcinoma by homologous targeting combined with oxygen transport. *Adv Sci*. 2023;10(5):e2203742. doi:10.1002/advs.202203742
37. Mueser TC, Rogers PH, Arnone A. Interface sliding as illustrated by the multiple quaternary structures of liganded hemoglobin. *Biochemistry*. 2000;39(50):15353–15364. doi:10.1021/bi0012944
38. Xia Y, Wang K, Zhao J, et al. Receptor tyrosine kinase fusion-mediated resistance to EGFR TKI in EGFR-mutant NSCLC: a multi-center analysis and literature review. *J Thorac Oncol*. 2024;S1556-0864(24):02490 doi:10.1016/j.jtho.2024.11.027.
39. Ji Q, Zhu H, Qin Y, et al. GP60 and SPARC as albumin receptors: key targeted sites for the delivery of antitumor drugs. *Front Pharmacol*. 2024;15:1329636. doi:10.3389/fphar.2024.1329636
40. Vogel SM, Minshall RD, Pilipović M, Tiruppathi C, Malik AB. Albumin uptake and transcytosis in endothelial cells in vivo induced by albumin-binding protein. *Am J Physiol Lung Cell Mol Physiol*. 2001;281(6):L1512–L1522. doi:10.1152/ajplung.2001.281.6.L1512
41. Maeda H, Wu J, Sawa T, Matsumura Y, Hori K. Tumor vascular permeability and the EPR effect in macromolecular therapeutics: a review. *J Control Release*. 2000;65(1–2):271–284. doi:10.1016/S0168-3659(99)00248-5
42. Aguilera KY, Brekken RA. Hypoxia studies with pimonidazole in vivo. *Biol Protoc*. 2014;4(19):e1254. doi:10.21769/BioProtoc.1254